

Article

Precipitate Characterization in Model Al-Zn-Mg-(Cu) Alloys Using Small-Angle X-ray Scattering

Daniel Freiberg^{1,2,*}, Wenhui Zhu², Jun-Sang Park³, Jonathan D. Almer³ and Paul Sanders¹

¹ Materials Science & Engineering Department, Michigan Technological University, Houghton, MI 49931, USA; sanders@mtu.edu

² Research and Innovation Center, Ford Motor Company, Dearborn, MI 48121, USA; wzhu45@ford.com

³ Argonne National Laboratory, Advanced Photon Source, Lemont, IL 60439, USA; parkjs@anl.gov (J.-S.P.); almer@anl.gov (J.D.A.)

* Correspondence: dfreiber@ford.com; Tel.: +1-313-269-3080

Received: 8 June 2020; Accepted: 13 July 2020; Published: 16 July 2020



Abstract: Model 7000 series alloys with and without copper were fabricated into sheets to study precipitation hardening behavior under isothermal aging conditions. Samples of each alloy were subjected to 3 h annealing treatments at various temperatures to produce a range of precipitate size distributions. Hardness, electrical conductivity, and small-angle X-ray scattering (SAXS) were used to characterize the aging behavior of the two alloys. Precipitate size distributions were modeled from the scattering curves for each annealing condition using a maximum entropy method (MEM) and compared to select transmission electron microscopy (TEM) results. The measured average precipitate diameters from TEM were in good agreement with the average precipitate diameters determined from the scattering curves.

Keywords: small-angle X-ray scattering; SAXS; maximum entropy method; 7000 series; precipitate

1. Introduction

The 7000 series alloys based on the Al-Zn-Mg-(Cu) system are used for high-strength structural components in aerospace, automotive, and military applications. These precipitation-hardenable alloys exhibit tensile yield strengths approaching 600 MPa due to densely distributed nano-sized precipitates formed during artificial aging [1].

The precipitation sequence in 7000 series alloys—like other precipitation-strengthened alloys—is influenced by alloy chemistry, thermo-mechanical processing, and final age hardening heat treatments. The Zn:Mg ratio, Cu content, homogenization and rolling practice, and aging practice collectively determine the final volume fraction and spatial distribution of precipitates in Al-Zn-Mg-(Cu) alloys [2].

Precipitates typically observed in artificially aged 7000 series alloys without Cu (Al-Zn-Mg) include the equilibrium η (MgZn_2) phase and its precursor η' phase. In artificially aged 7000 series alloys with Cu (Al-Zn-Mg-Cu), observed precipitates are the equilibrium η phase expressed as $\text{Mg}(\text{Zn,Cu,Al})_2$ and its precursor η' phase [3]. In general, the precipitation sequence in Al-Zn-Mg-(Cu) alloys begins with the decomposition of a supersaturated solid solution (SSSS) into nano-sized (~ 3 nm) clusters of Mg and Zn atoms called Guinier-Preston (GP) zones. Two types of GP zones can form depending on quenching and aging conditions: spherical GPI zones or plate-like GPII zones [4]; both types impede dislocation movement and thus increase strength. GP zones evolve into the metastable ellipsoidal η' strengthening phase that is semi-coherent with the aluminum matrix [2,5,6]. Upon further aging, the η' evolves into the equilibrium η phase [6].

Precipitation in metallic alloys causes local composition fluctuations as precipitates nucleate and grow. Small-angle X-ray scattering (SAXS) signals are sensitive to local changes in electron density or

atomic number, and thus SAXS is sensitive to local changes in composition and can be used to study precipitate evolution.

High-energy synchrotron X-ray sources enable SAXS experiments on metallic alloys. For sheet materials, SAXS experiments can be run in transmission mode, where the incident X-ray beam passes through the sample. The scattered X-ray signal can be analyzed to determine the precipitate size and volume fraction [7,8]. The scattered signal or intensity I is measured as a function of the scattering vector q .

$$|q| = 4\pi \sin(\theta) / \lambda \quad (1)$$

For synchrotron experiments, the X-ray wavelength λ is often fixed. In SAXS experiments, the scattering angle 2θ can range from 0.1 to 6°. The scattering angle is determined by the distance between the sample and the detector as well as the detector size and the beam stop position. In transmission mode, the scattered intensity is recorded as a two-dimensional image. The two-dimensional scattering image is radially averaged, producing a one-dimensional scattering curve of intensity I vs. scattering vector q .

The measured scattering signal $I(q)$ is proportional to the squared difference between the scattering length densities of the scatterer $\rho_{e,scatterer}$, and matrix $\rho_{e,matrix}$.

$$I(q) \propto |\Delta\rho|^2 = |\rho_{e,scatterer} - \rho_{e,matrix}|^2 \quad (2)$$

Scattering length density is related to atomic number. SAXS is most effective when the difference between the atomic number Z of a scatterer and the atomic number of the matrix is large. The study of precipitation in 7000 series alloys is well suited for SAXS because there is a high electron density contrast between zinc-bearing precipitates ($Z_{Zn} = 30$) and the aluminum ($Z_{Al} = 13$) matrix.

The average precipitate size and volume fraction can be extracted from the scattering curves. The precipitate size and volume fraction information can be used to predict the strength contributed by precipitation hardening.

2. Materials and Methods

2.1. Material Processing

Two model 7000 series alloys were cast and rolled into sheet material at Michigan Technological University's pilot-scale casting and thermo-mechanical processing facility. The alloys were cast into 18-mm-thick plates using a chemically bonded sand mold with integrated Cu chill, as schematically shown in Figure 1. The chemical compositions for the non-copper and copper-containing model 7000 series alloys were determined by inductively coupled plasma optical emission spectroscopy (ICP-OES) (Table 1).

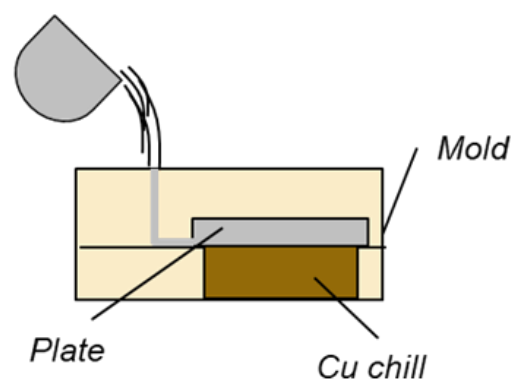


Figure 1. Schematic cross section of chemically bonded sand mold with integrated copper chill used to produce cast plates.

Table 1. Chemical composition determined by ICP-OES (wt.%).

Alloy	Al	Mn	Zn	Cu	Mg	Fe
Al-Zn-Mg	Balance	0.001	6.38	0.006	2.96	<0.01
Al-Zn-Mg-Cu	Balance	0.002	6.24	2.05	2.68	<0.01

Both alloys were homogenized at 450 °C for 24 h. The homogenized plates were hot-rolled at 400 °C to 4 mm thickness with 1 mm thickness reduction per roll pass—plates were re-heated to 400 °C prior to each roll pass. The hot-rolled material was cold-rolled to a final thickness of 3 mm. The cold-rolled material was then solution heat treated at 470 °C for 1 h, followed immediately by a water quench. Coupons from the Al-Zn-Mg and Al-Zn-Mg-Cu alloys were naturally aged at room temperature for 24 h, then artificially aged for 3 h at 100, 120, 140, 160, 180, or 200 °C. Rockwell (B-scale) hardness and eddy current electrical conductivity were measured after each isothermal heat treatment to characterize precipitation as a function of isothermal aging temperature.

2.2. Small-Angle X-ray Scattering Experiment and Analysis Method

A synchrotron-based small-angle X-ray scattering (SAXS) experiment was performed at beamline 1-ID at Argonne National Lab (ANL)—Advanced Photon Source (APS). Ex-situ SAXS samples were prepared from each isothermal aging condition from the copper and non-copper alloys. Discs, 7.5 mm in diameter, were electro-discharge machined (EDM'd) from the 3 mm sheet and loaded into a wheel sample fixture (Figure 2). A beam energy of 71.676 keV and a beam size of 150 $\mu\text{m} \times 150 \mu\text{m}$ was used to probe the aluminum samples in the wheel fixture. A Pixirad 2 detector equipped with PIXI III ASICs (Pixirad Imaging Counters S.R.L., Verona, Italy) was used to measure scattering intensity over a q range of approximately 0.01–0.35 \AA^{-1} , allowing for the detection of microstructural features such as GP zones $\sim 10 \text{\AA}$ in diameter and coarse precipitates $\sim 600 \text{\AA}$ in diameter. Raw two-dimensional intensity data was radially averaged and corrected to give absolute intensity units (cm^{-1}) vs. q (\AA^{-1}) for each artificial aging condition. Absolute intensity calibration was verified using a glassy carbon standard [9]. Figure 3 shows absolute intensity vs. q for the glassy carbon sample measured in this SAXS experiment (red curve) compared to the glassy carbon sample (green curve) previously measured with ultra-small-angle X-ray scattering (USAXS) at APS [9].

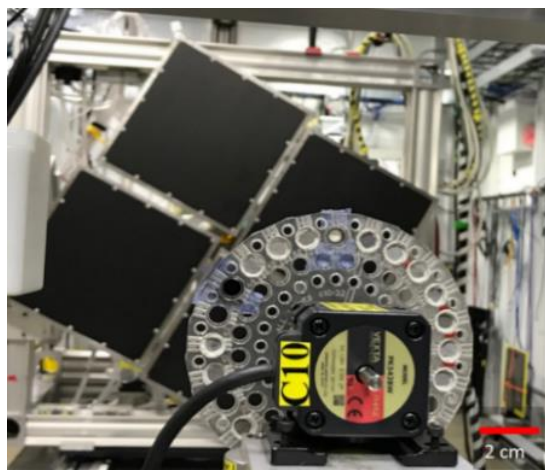


Figure 2. Wheel sample fixture used to hold and index samples during SAXS experiment.

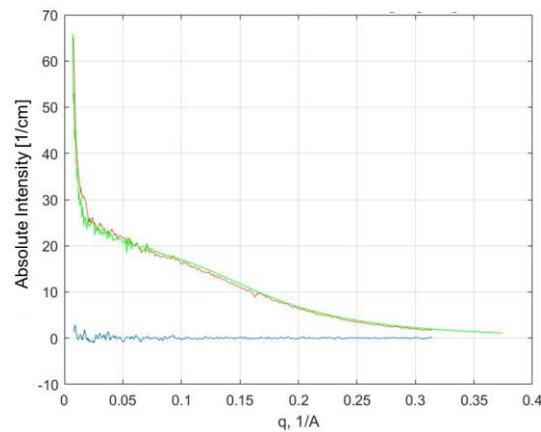


Figure 3. Lineouts showing absolute intensity vs. q measurements from glassy carbon sample from this SAXS experiment (red) and absolute intensity vs. q measurements from glassy carbon sample measured using USAXS; blue curve is air, shown for reference.

The measured intensity I is related to the spatial distribution of scatterers and the characteristic shape of the scatterer. If the general shape of the scatterer—or, in this case—if the general shape of the precipitate is known, then information about precipitate size can be extracted by solving for the unknown particle size distribution $x_T(D)$ in,

$$I = \int_0^{\infty} G(q, D)x_T(D)dD \quad (3)$$

where $G(q, D)$ represents the scattering function at the scattering vector q of a single scatterer with a characteristic shape [10]. For this work, precipitates (i.e., scatterers) were modeled as a spheroid with an aspect ratio of 1.7—this morphology and aspect ratio was verified with TEM precipitate size measurements. The unknown particle size distribution $x_T(D)$ was determined from each scattering curve (I vs. q) using the size distribution model in GSAS-II software (revision 3957, UChicago Argonne LLC, Chicago, IL, USA) [11,12]. The model uses a maximum entropy routine that compares measured intensities on a scattering curve to corresponding intensities calculated for a range of user-defined particle sizes [10,13,14]. The unknown particle size distribution for each heat treatment condition was reported as the volume distribution of particle sizes. The average precipitate diameter was computed from generated volume distribution plots.

The integrated intensity or scattering invariant Q_0 from the scattering curves is proportional to the precipitate volume fraction. The scattering invariant Q_0 can be computed using the following:

$$Q_0 = \int_0^{\infty} Iq^2dq \quad (4)$$

where I is the measured absolute intensity and q is the scattering vector. The integrated intensity (scattering invariant) can be used to compute the precipitate volume fraction f_V in Al-Zn-Mg-(Cu) alloys using the following equation from Deschamps et al. [15]:

$$Q_0 = 2\pi^2 f_V(1 - f_V)(\Delta\rho)^2 \approx \frac{2\pi^2 f_V(1 - f_V)(Z_p - Z_m)^2}{\Omega^2} \quad (5)$$

where Q_0 is the scattering invariant, f_V is the precipitate volume fraction, Z_p and Z_m are the average atomic numbers of the precipitate and matrix, and Ω is the atomic volume of the precipitate (approximated as 16.5 \AA^3) [5]. The average atomic numbers of the precipitate and matrix were computed as a function of the precipitate composition and matrix composition, respectively. The precipitate composition and

matrix composition were taken from the Deschamps et al. tomographic atom probe (TAP) measurements in [15].

The precipitate volume fraction and average precipitate size determined from SAXS were used to estimate the precipitate strengthening contribution in both alloys after each heat treatment condition. Strength was calculated for the cases of pure shear and pure by-pass using equations from [16]. For the pure shear case, the following equation was used:

$$Q_0 = 2\pi^2 f_V (1 - f_V) (\Delta\rho)^2 \approx \frac{2\pi^2 f_V (1 - f_V) (Z_P - Z_m)^2}{\Omega^2} \quad (6)$$

and the for the pure by-pass case, the following equation was used:

$$\sigma_b = \sqrt{\frac{6}{\pi}} \beta M \mu b \frac{f_V^{1/2}}{R} \quad (7)$$

where M is the Taylor factor, β and μ are phenomenological parameters, k is an adjustable fitting parameter, f_V is the precipitate volume fraction, and R is the precipitate radius. In the pure shear case, moving dislocations cut through precipitates, whereas in the pure by-pass case, moving dislocations maneuver around or by-pass precipitates.

2.3. TEM Experimental Setup and Analysis Method

TEM samples were prepared from the Al-Zn-Mg and Al-Zn-Mg-Cu alloys at select artificial aging conditions. The samples were ground and polished in the rolling plane to approximately 100- μ m-thick foils. Discs, 3 mm in diameter, were punched from the foils, dimpled to approximately 30–50 μ m thickness, and ion milled until perforation. The as-prepared TEM specimens were examined with a Talos F200X TEM (Thermo Fisher Scientific, Hillsboro, OR, USA) operated at 200 kV. Selected area diffraction pattern (SADP) images, as well as bright field and high-resolution transmission electron microscopy (HRTEM) images, were taken in the $\langle 110 \rangle$ zone axis. ImageJ (1.51, National Institutes of Health, Bethesda, MD, USA) [17] was used to measure the average precipitate diameter from the bright field and HRTEM images. Three to five images from different locations on each TEM specimen were used to measure the diameter of at least 100 precipitates—diameter was taken as the length across the minor axis of the precipitate. Both major and minor axis lengths were measured to inform the 1.7 aspect ratio used in the GSAS-II size distribution model.

3. Results and Discussion

Hardness and electrical conductivity vs. heat treatment conditions are displayed in Figure 4 for the Al-Zn-Mg and Al-Zn-Mg-Cu alloys. Both alloys reached a peak hardness after 3 h at 140 °C (Figure 4a). The copper-bearing alloy had a greater peak hardness after 140 °C/3 h compared to the non-Cu-bearing alloy (90 vs. 85 HRb). For the Cu-bearing alloy only, the hardness appeared to plateau with very little change between the 120, 140, and 160 °C isothermal heat treatments.

As-quenched hardness (13 HRb) for the Al-Zn-Mg alloy (Figure 4a) was lower than the as-quenched hardness (57 HRb) for the Al-Zn-Mg-Cu alloy (Figure 4a). After 24 h of natural aging, the Al-Zn-Mg alloy gained considerable strength, as indicated by the sharp increase in hardness from 13 to 52 HRb (Figure 4a). Chinh et al. [18] concluded that Cu-bearing vacancy-rich clusters (VRCs) can form immediately after quenching, offering a significantly greater strengthening effect than VRCs formed in ternary Al-Zn-Mg alloys. These Cu-bearing VRCs may explain the large difference in the observed as-quenched hardness since more VRCs would result in more GP zones and higher strength.

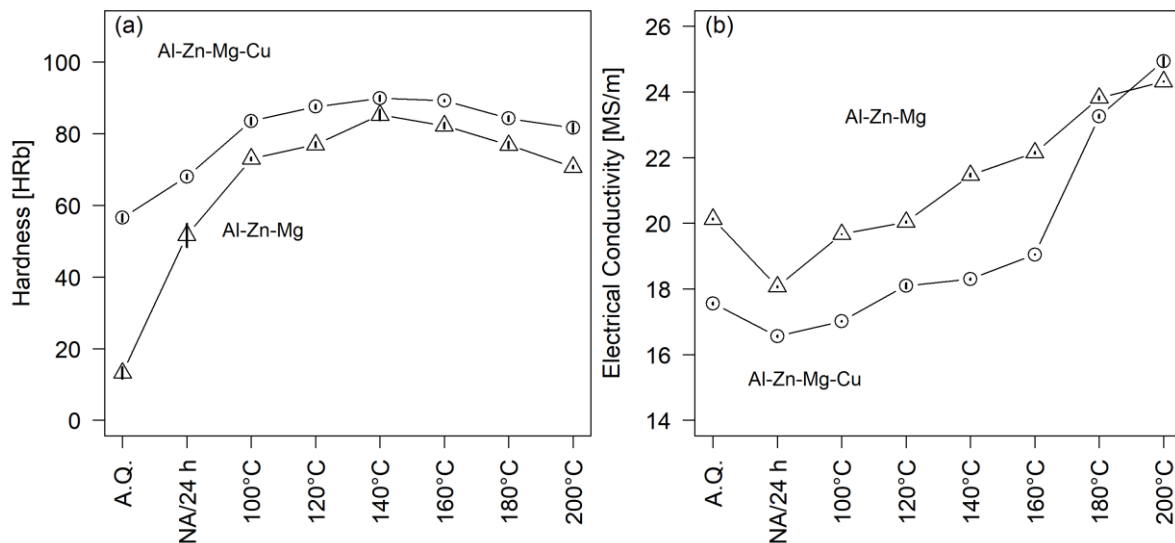


Figure 4. (a) Rockwell B hardness (HRb) for Al-Zn-Mg (triangles) and Al-Zn-Mg-Cu (circles) alloys for multiple conditions: as-quenched (A.Q.); natural aged for 24 h (NA); and isothermal annealing treatments from 100 to 200 °C (each treatment was 3 h). (b) Electrical conductivity (MS/m) for Al-Zn-Mg (triangles) and Al-Zn-Mg-Cu (circles) alloys for multiple conditions: as-quenched; 24 h of natural age (NA); 3 h isothermal annealing treatments from 100 to 200 °C. Error bars equal the 95% confidence interval of the mean.

In both alloys, regardless of copper content, natural aging after quench resulted in increased hardness and decreased electrical conductivity (Figure 4b). This confirmed GP zone formation, as GP zones impede dislocation movement and are thought to impair lattice periodicity, resulting in more restrictive electron movement, and thus reduced conductivity [19]. In contrast, conductivity increased with increasing heat treatment temperature for both Cu- and non-Cu-containing alloys. The increase in conductivity was due to the decomposition of the solid solution into precipitates. Solute in solid solutions tends to restrict electron movement. As solutes leave solid solution and form precipitates, electrons tend to move more freely throughout the aluminum matrix, resulting in increased electrical conductivity.

Figure 5 shows TEM images of the two alloys after the 120 °C and 160 °C 3 h isothermal heat treatments. After the 160 °C/3 h treatment, η'/η phases were observed in the aluminum matrix for both the Al-Zn-Mg (Figure 5a) and Al-Zn-Mg-Cu (Figure 5b) alloys. Precipitates in the Al-Zn-Mg alloy after the 120 °C/3 h treatment (Figure 5c) had little contrast, making observation difficult. However, the HRTEM inset image in Figure 5c shows evidence of coherent GP zones as dark agglomerates, with similar lattice structure to the surrounding light-gray aluminum matrix. Precipitates can be clearly observed in the TEM image of the Al-Zn-Mg-Cu alloy after the 120 °C/3 h treatment (Figure 5d). The HRTEM inset shows that these precipitates were coherent GP zones, indicated by the similarity in lattice structure between the dark contrast areas and light-gray aluminum matrix (Figure 5d). In summary, TEM observations indicated that GP zones were present after the 120 °C/3 h heat treatment for both the non-Cu- and Cu-containing alloys. After the 160 °C/3 h treatment, η'/η precipitates were observed in both alloys.

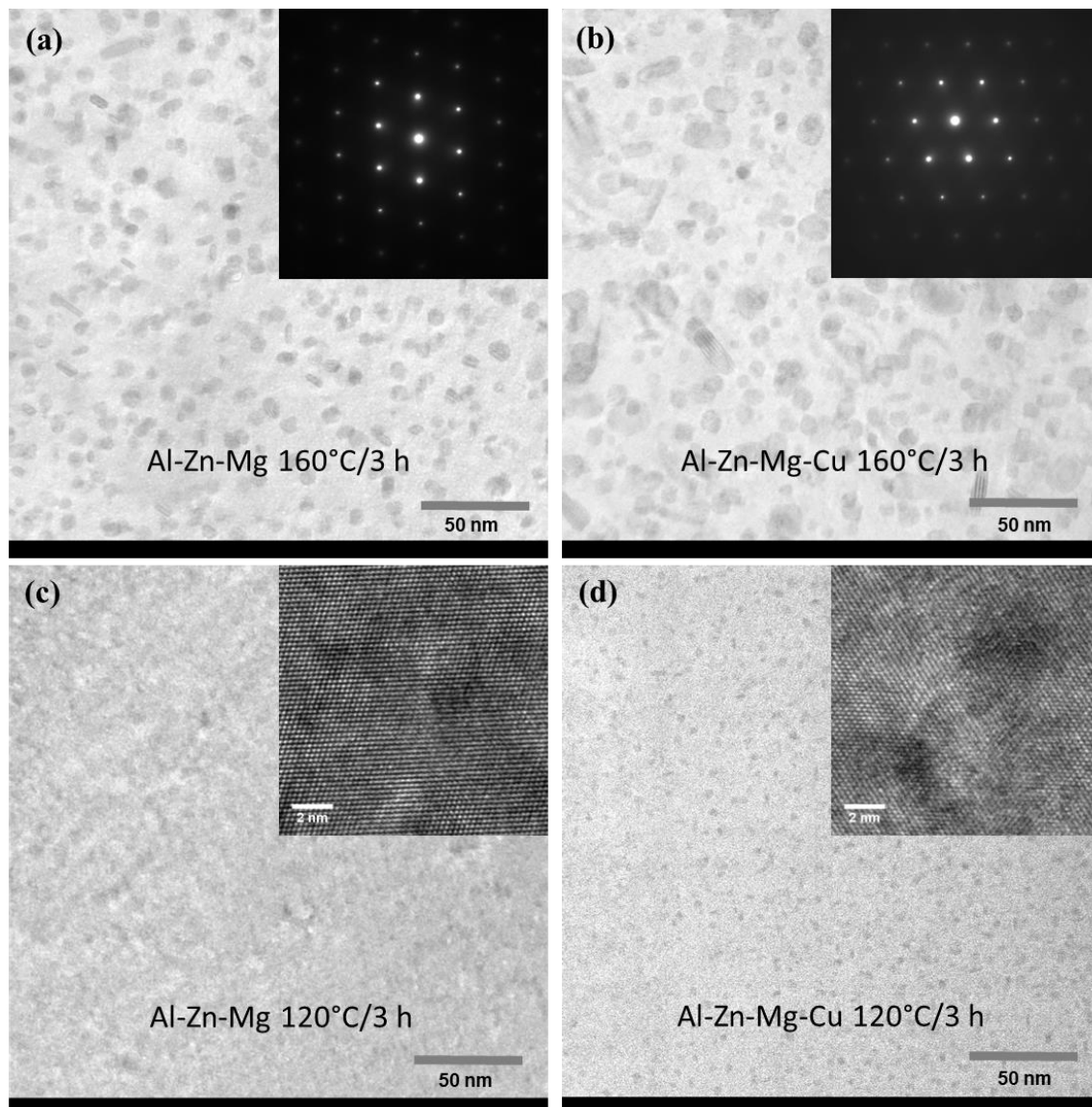


Figure 5. TEM images of (a) Al-Zn-Mg alloy after 160 °C/3 h, with inset of SADP of Al $\langle 011 \rangle$, (b) Al-Zn-Mg-Cu alloy after 160 °C/3 h with inset of SADP of Al $\langle 011 \rangle$, (c) Al-Zn-Mg alloy after 120 °C/3 h, with inset of HRTEM image showing coherent interface between precipitates (dark globular features) and Al matrix, (d) Al-Zn-Mg-Cu alloy after 120 °C/3 h, with HRTEM image as an inset, showing coherent interface between precipitates (dark globular features) and Al matrix.

The scattering curves for each 3 h isothermal heat treatment are plotted for the Al-Zn-Mg and Al-Zn-Mg-Cu alloys in Figure 6. The scattering curves from the Al-Zn-Mg-Cu alloy are plotted in Figure 6a,b, for 100, 120, and 140 °C isothermal heat treatments (Figure 6a) and 160, 180, and 200 °C heat treatments (Figure 6b). The scattering curves for the non-Cu-containing Al-Zn-Mg alloy are plotted in Figure 6c,d for 100, 120, and 140 °C isothermal heat treatments (Figure 6c) and 160, 180, and 200 °C heat treatments (Figure 6d). The scattered intensity at the high q -range is due to small precipitates such as GP zones and small, early-stage η' precipitates. Scattered intensity at the low q -range is due to larger precipitates such as η' and η phases. As isothermal heat treatment temperature increased, the curves shifted to lower q -range values and higher intensities as the precipitate size and volume fraction increased.

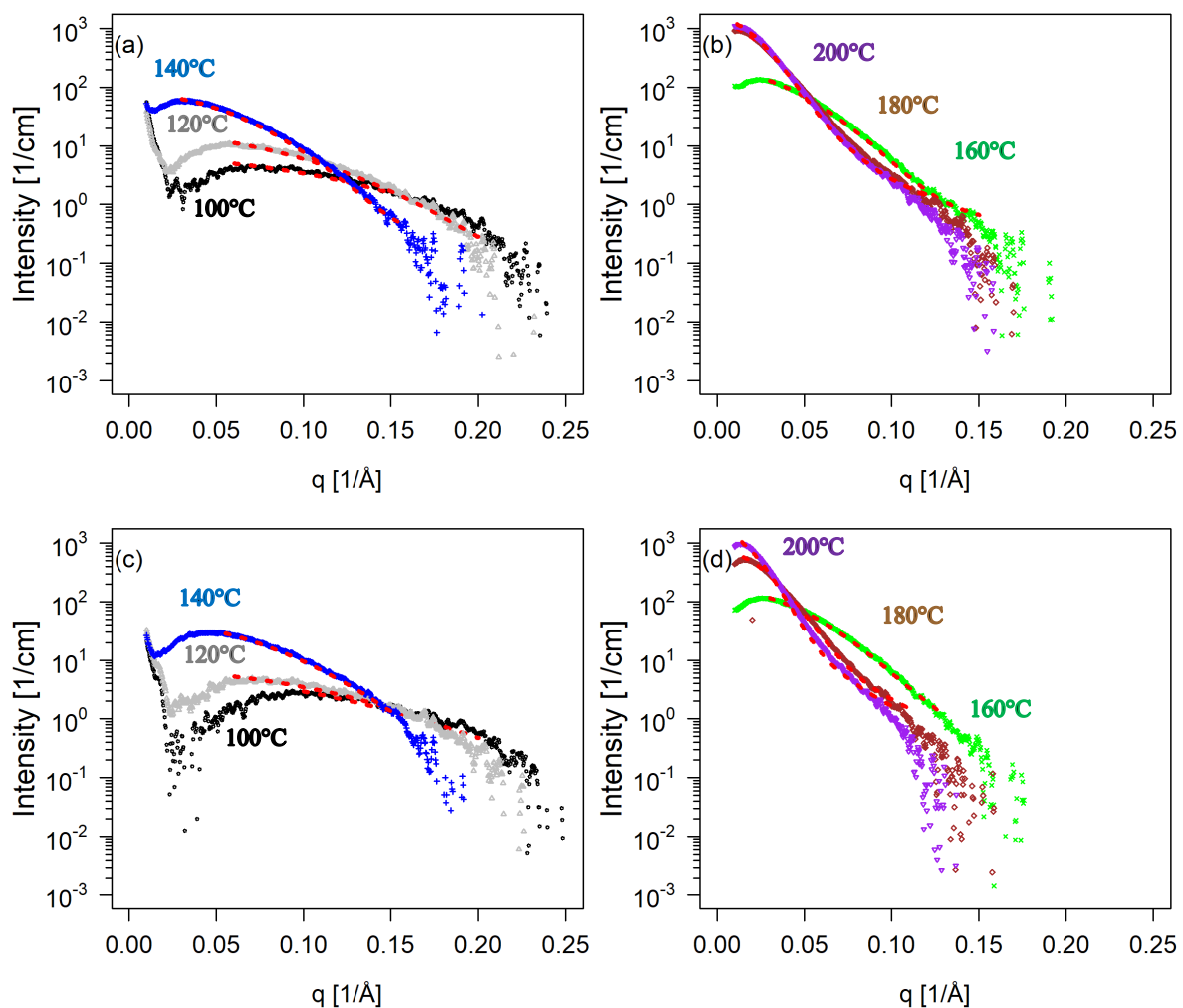


Figure 6. Small-angle X-ray scattering (SAXS) intensity I vs. scattering vector q for (a) Al-Zn-Mg-Cu after 100, 120, and 140 °C 3 h isothermal heat treatments; (b) Al-Zn-Mg-Cu alloy after 160, 180, and 200 °C 3 h isothermal heat treatments; (c) Al-Zn-Mg after 100, 120, and 140 °C 3 h isothermal heat treatments; and (d) Al-Zn-Mg alloy after 160, 180, and 200 °C 3 h isothermal heat treatments.

For the scattering curves at lower temperatures (e.g., 100 °C, 120 °C, 140 °C), the curves begin with a sharp decline in intensity at low q , then rise to a maximum, followed by a gradual decline in intensity. This initial dip in intensity at low q is caused by a destructive interference effect due to high precipitate number densities [8]. This initial intensity dip was filtered out prior to modeling the precipitate size distribution using the GSAS-II maximum entropy method. The red dashed lines overlaid on the scattering curves in Figure 6 represent the portion of the scattering curve that was modeled using the maximum entropy method. The particle size distributions were calculated from these best-fit functions.

The average precipitate diameter determined from the SAXS-MEM is plotted for each artificial age condition for the non-Cu- and Cu-containing alloys in Figure 7. The solid points plotted in Figure 7 are the average precipitate diameters measured from the TEM images, which are in good agreement with the SAXS measurements. The calculated precipitate volume fraction is shown in Figure 8. The volume fraction for the Cu-containing alloy was higher than the non-Cu alloy at low heat treatment temperatures (i.e., 100 °C, 120 °C). After the 140 °C and 160 °C heat treatments, both alloys had nearly the same volume fraction. The volume fractions in both alloys plateaued after the 180 °C and 200 °C heat treatments. The Cu-containing alloy had about a 20% higher volume fraction than the non-Cu alloy after the 180 °C and 200 °C heat treatments.

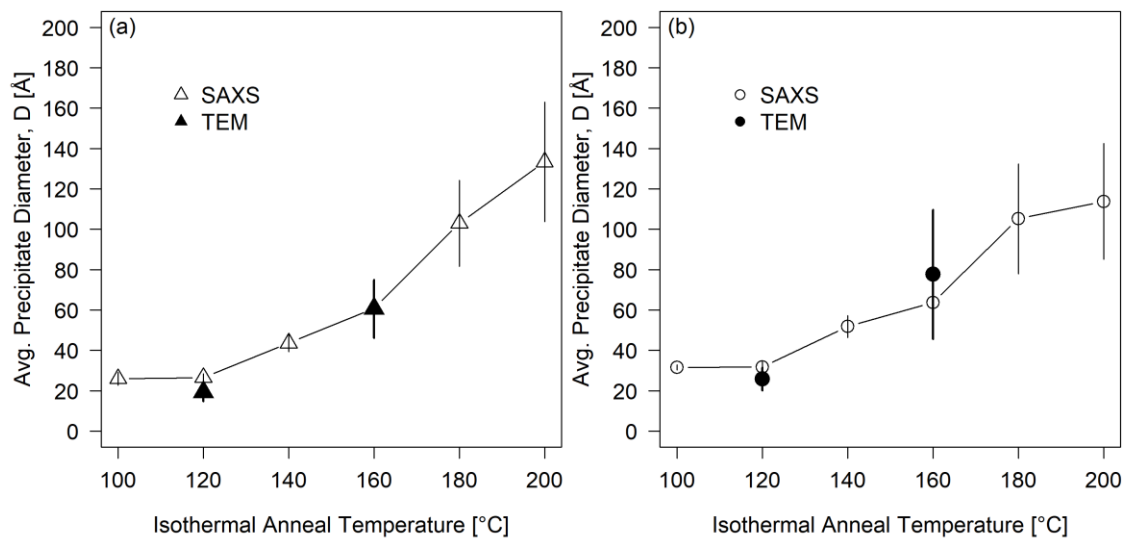


Figure 7. Average precipitate diameters as a function of isothermal anneal temperature for (a) Al-Zn-Mg alloy and (b) Al-Zn-Mg-Cu alloy; open points are SAXS precipitate measurements and solid points are TEM precipitate measurements; error bars show one standard deviation of the mean.

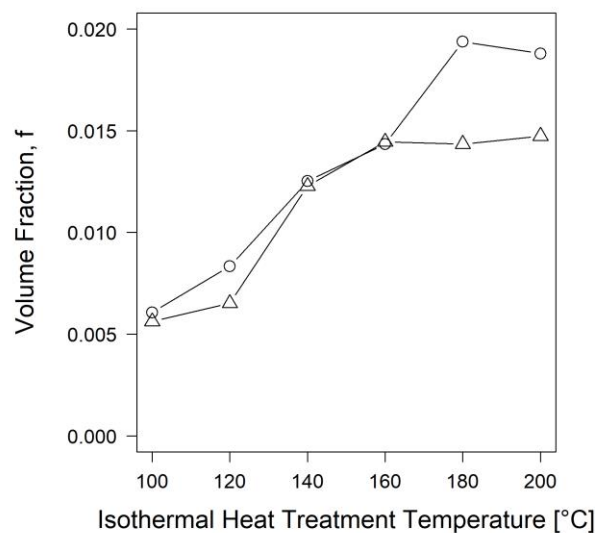


Figure 8. Calculated precipitate volume fraction for Al-Zn-Mg (triangles) and Al-Zn-Mg-Cu (circles) alloys after various 3 h isothermal heat treatments.

Figure 9 shows the calculated strength increase due to precipitation hardening for both pure shear and pure by-pass mechanisms. The strength increase was calculated for each case using Equations (6) and (7); the precipitate size and volume fraction measurements presented in Figures 6 and 7 were used as inputs. The strength of a precipitation-hardenable alloy is governed by the interaction of the dislocations with the precipitates. Dislocations interact with precipitates by two mechanisms: (1) shearing or (2) by-pass. In the under-aged condition, the shearing mechanism is dominant—where strength increase due to precipitation hardening $\Delta\sigma$ is proportional to the precipitate volume fraction f_V and average precipitate radius R ,

$$\Delta\sigma \propto (f_V R)^{1/2} \quad (8)$$

Here, precipitate size is proportional to strength. Precipitates are shearable in the under-aged condition up to a critical radius. When precipitate size grows beyond the critical radius, then the Orowan strengthening mechanism becomes dominant. Instead of shearing, the dislocations bow around and by-pass precipitates. This is called Orowan strengthening, where $\Delta\sigma$ is proportional to f_V and R by:

$$\Delta\sigma \propto \frac{f_V^{1/2}}{R} \quad (9)$$

Precipitates in the over-aged condition are non-shearable, and strength is controlled by the Orowan mechanism, where material strength is inversely proportional to precipitate size.

The transition from shear to by-pass mechanism occurs around the 140 °C heat treatment temperature for both Al-Zn-Mg and Al-Zn-Mg-Cu alloys. Precipitate shearing is the dominant strengthening mechanism after the 100 and 120 °C heat treatments, whereas the by-pass mechanism becomes dominant after the 160, 180, and 200 °C heat treatments.

Peak strength in precipitation-hardenable alloys occurs at the transition from shearing to by-pass. Peak hardness (strength) was observed after the 140 °C/3 h heat treatment for the Cu-bearing and non-Cu-bearing alloys in Figure 4a. The point at which peak hardness is observed in Figure 4a agrees well with the calculations in Figure 9, which shows that the transition from shearing to by-pass mechanism occurs around 140 °C.

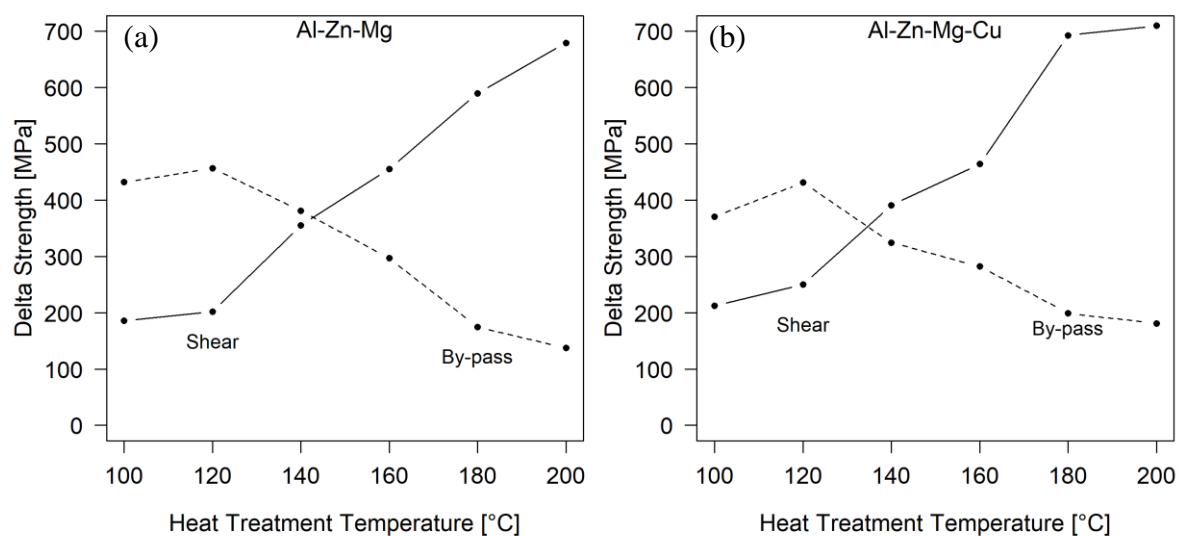


Figure 9. Estimated delta strength from shearing and by-pass precipitation hardening mechanisms for (a) Al-Zn-Mg alloy and (b) Al-Zn-Mg-Cu alloys after various 3 h isothermal heat treatments.

The average precipitate diameter measured from the SAXS data for the 140 °C/3 h heat treatment was 44 ± 4 Å for the non-Cu alloy and 52 ± 5 Å for the Cu-containing alloy. Assuming these measurements are respective of critical precipitate size, the transition from shearing to Orowan type strengthening mechanism occurred at larger precipitate sizes in the Cu-containing Al-Zn-Mg-Cu alloy. Hardness began to decrease after the 160 °C aging treatment for both alloys, followed by further decline after the 180 °C and 200 °C heat treatments (Figure 4a). Similarly, the calculated strength delta in Figure 9 decreases after the 160 °C heat treatment. As the hardness decreases, precipitates continue to coarsen, indicated by an increase in average precipitate size for both alloys in Figure 7.

4. Conclusions

Two model Al-Zn-Mg and Al-Zn-Mg-Cu alloys were cast and fabricated into sheet material and given 3 h isothermal heat treatments ranging in temperature from 100 to 200 °C. The average precipitate diameter and precipitate volume fraction were characterized for each heat treatment condition using synchrotron-based small-angle X-ray scattering. A maximum entropy method (MEM) was used to determine the average precipitate diameter from SAXS intensity vs. q curves for each heat treatment condition. SAXS precipitate diameter measurements were verified with TEM precipitate diameter measurements for two conditions: 120 °C/3 h and 160 °C/3 h. TEM precipitate diameter measurements were in good agreement with SAXS precipitate diameter measurements. The precipitate volume

fraction was computed from the integrated intensity. The measured precipitate size and volume fraction were used to calculate the change in strength due to precipitates. The transition from shearing mechanisms to by-pass mechanisms from the calculations agreed well with the observed peak hardness measurements for both alloys.

Author Contributions: Conceptualization, D.F., P.S.; methodology, D.F., W.Z., P.S., J.-S.P., J.D.A.; data curation, J.-S.P., J.D.A., W.Z.; formal analysis, D.F.; writing—original draft preparation, D.F.; writing—review and editing, W.Z., P.S., D.F.; supervision, P.S. All authors have read and agreed to the published version of the manuscript.

Funding: This research received no external funding.

Acknowledgments: The authors would like to thank the beamline 1-ID staff at Argonne National Lab Advanced Photon Source for performing the SAXS experiment. Many thanks to Thomas Wood and Devin Deaton at Michigan Technological University for helping with the fabrication and characterization of the alloys.

Conflicts of Interest: The authors declare no conflicts of interest.

References

1. Poznak, A.; Freiberg, D.; Sanders, P. Chapter 10—Automotive Wrought Aluminium Alloys. In *Fundamentals of Aluminium Metallurgy*; Lumley, R., Ed.; Elsevier: Duxford, UK, 2018; pp. 333–386.
2. Azarniya, A.; Taheri, A.K.; Taheri, K.K. Recent advances in ageing of 7xxx series aluminum alloys: A physical metallurgy perspective. *J. Alloys Compd.* **2019**, *781*, 945–983. [[CrossRef](#)]
3. Starke, E.A.; Staley, J.T. 24—Application of modern aluminium alloys to aircraft. In *Fundamentals of Aluminium Metallurgy*; Lumley, R., Ed.; Woodhead Publishing: Cambridge, UK, 2011; pp. 747–783.
4. Berg, L.K.; Gjønnes, J.; Hansen, V.; Li, X.Z.; Knutson-Wedel, M.; Waterloo, G.; Schryvers, D.; Wallenberg, L.R. GP-zones in Al–Zn–Mg alloys and their role in artificial aging. *Acta Mater.* **2001**, *49*, 3443–3451. [[CrossRef](#)]
5. Du, Z.W.; Sun, Z.M.; Shao, B.L.; Zhou, T.T.; Chen, C.Q. Quantitative evaluation of precipitates in an Al–Zn–Mg–Cu alloy after isothermal aging. *Mater. Charact.* **2006**, *56*, 121–128. [[CrossRef](#)]
6. Xu, X.; Zheng, J.; Li, Z.; Luo, R.; Chen, B. Precipitation in an Al–Zn–Mg–Cu alloy during isothermal aging: Atomic-scale HAADF–STEM investigation. *Mater. Sci. Eng. A* **2017**, *691*, 60–70. [[CrossRef](#)]
7. Guinier, A.; Fournet, G. *Small Angle Scattering of X-Rays*. John Wiley & Sons: New York, NY, USA, 1955.
8. De Geuser, F.; Deschamps, A. Precipitate characterisation in metallic systems by small-angle X-ray or neutron scattering. *Comptes Rendus Phys.* **2012**, *13*, 246–256. [[CrossRef](#)]
9. Zhang, F.; Ilavsky, J.; Long, G.G.; Quintana, J.P.G.; Allen, A.J.; Jemian, P.R. Glassy carbon as an absolute intensity calibration standard for small-angle scattering. *Metall. Mater. Trans. Phys. Metall. Mater. Sci.* **2010**, *41*, 1151–1158. [[CrossRef](#)]
10. Jemian, P.R.; Weertman, J.R.; Long, G.G.; Spal, R.D. Characterization of 9Cr–1MoVNb Steel by Anomalous Small-Angle X-Ray Scattering. *Acta Metall. Mater.* **1991**, *39*, 2477–2487. [[CrossRef](#)]
11. Toby, B.H.; Von Dreele, R.B. GSAS-II: The genesis of a modern open-source all purpose crystallography software package. *J. Appl. Crystallogr.* **2013**, *46*, 544–549. [[CrossRef](#)]
12. Von Dreele, R.B. Small-angle scattering data analysis in GSAS-II. *J. Appl. Crystallogr.* **2014**, *47*, 1784–1789. [[CrossRef](#)]
13. Potton, J.A.; Daniell, G.J.; Rainford, B.D. Particle size distributions from SANS data using the maximum entropy method. *J. Appl. Crystallogr.* **1988**, *21*, 663. [[CrossRef](#)]
14. Potton, J.A.; Daniell, G.J.; Rainford, B.D. Application of maximum entropy to small-angle neutron scattering data and liquid and amorphous material diffraction data analysis. *Inst. Phys. Conf. Ser.* **1986**, *81*, 81.
15. Deschamps, A.; Bigot, A.; Livet, F.; Auger, P.; Bréchet, Y.; Blavette, D. A comparative study of precipitate composition and volume fraction in an Al–Zn–Mg alloy using tomographic atom probe and small-angle X-ray scattering. *Philos. Mag. A* **2001**, *81*, 2391–2414. [[CrossRef](#)]
16. Deschamps, A.; Bréchet, Y. Influence of Predeformation and Ageing of an Al–Zn–Mg Alloy—Modeling of Precipitation Kinetics and Yield Stress. *Acta Metall.* **1998**, *47*, 293–305. [[CrossRef](#)]
17. Rasband, W. ImageJ. National Institutes of Health, USA. Available online: <https://imagej.net/Welcome> (accessed on 8 June 2020).
18. Chinh, N.Q.; Lendvai, J.; Ping, D.H.; Hono, K. The effect of Cu on mechanical and precipitation properties of Al–Zn–Mg alloys. *J. Alloys Compd.* **2004**, *378*, 52–60. [[CrossRef](#)]

19. Hunsicker, H.Y. Metallurgy of Heat Treatment. In *Aluminum: Properties and Physical Metallurgy*; ASM International: Cleveland, OH, USA, 1984.



© 2020 by the authors. Licensee MDPI, Basel, Switzerland. This article is an open access article distributed under the terms and conditions of the Creative Commons Attribution (CC BY) license (<http://creativecommons.org/licenses/by/4.0/>).